Mandilas, C.; Karagiannakis, G.; Lazzaro, M.; Beatrice, C.; Konstandopoulos, A.; Di Blasio, G.; Molina, S.... (2016). Study of Oxidation and Combustion Characteristics of Iron Nanoparticles under Idealized and Enginelike Conditions. Energy and Fuels. 30(5):4318-4330. doi:10.1021/acs.energyfuels.6b00121.

Study of oxidation and combustion characteristics of iron nanoparticles under idealized and engine-like conditions

Charalampos Mandilas[a], George Karagiannakis[a], Athanasios G. Konstandopoulos[a,b*], Carlo Beatrice[c], Maurizio Lazzaro[c], Gabriele Di Blasio[c], Santiago Molina[d], Josè V. Pastor[d] and Antonio Gil[d]*

[a] Aerosol & Particle Technology Laboratory (APTL), Chemical Process & Energy Resources Institute, Center for Research & Technology-Hellas (CERTH/CPERI), P.O. Box 361, 57001 Thermi-Thessaloniki, GREECE

[b] Department of Chemical Engineering, Aristotle University, P.O. Box 1517, 54006 Thessaloniki, GREECE

[c] Istituto Motori – CNR, Viale Marconi 81056 Naples, ITALY

[d] CMT-Motores Térmicos, Camino de Vera s/n,

46022, Universitat Politècnica de València, Valencia, SPAIN

*corresponding authors: agk@cperi.certh.gr, mandilas@cperi.certh.gr

(Tel: +302310498192, +302310498198)

Abstract

The present work includes findings from in-principle feasibility studies on iron nanopowder combustion under idealized, engine-like and real engine conditions. The study was conducted under the scope of recent interest of metallic nanoparticles as alternative fuels for Internal Combustion Engines (ICE). More specifically, Fe nanoparticles of different morphology and size were studied with respect to their oxidation characteristics via Thermo-Gravimetric Analysis (TGA), as well as in customized shock-tube, constant volume vessel and CI engine configurations. Combusted powder samples were, in all cases, examined via in-situ and ex-situ techniques for the identification of combustion products and their morphologies. Findings facilitated determination of the main phenomena involved during oxidation. The results verified that combustion of Fe nanoparticles in an engine environment is feasible. Notable differences in the morphological structure of the products formed were identified among the various oxidation/combustion techniques employed.

Keywords: iron combustion, nanoparticle combustion, metallic fuels, alternative fuels, metal fuelled engine

1. Introduction

The idea of metals as energy carriers for transport applications was introduced a few decades ago and principally lies on two fundamental characteristics. Firstly, some metals have significantly higher energy content per unit volume than carbon-based liquid fuels. Secondly, provided that the combustion process is properly controlled, the only product is the respective metal oxide. Thus, such a concept can be emission-free thereby enhancing the environmental friendliness of the particular approach. In principle, if combustion temperature is kept below the NO_x formation threshold, the

only product for complete oxidation would be the solid metal oxide. In the case of iron the overall reaction could be written as,

$$Fe + \tfrac{3}{4} O_2 \rightarrow \tfrac{1}{2} Fe_2O_3,\ \Delta H^o = -413.1\ kJ/mol \qquad (1)$$

Implicitly, all pollutants derived from the combustion process of conventional carbon based liquid fuels are avoided. The "green" nature of the concept can be further strengthened under the prerequisite that the metal oxide (spent fuel) is recycled so that the metal is recovered and reused.

Research towards a metal fuelled internal combustion engine (ICE) can only be realistic provided that the metal fuel itself is as manageable as possible, in terms of ignition, burn rate and flow characteristics. Metallic nanopowders, as opposed to metallic powders of micron-sized particles, could practically meet the above [1]. Moreover, recent progress in the quality (size distribution, purity, shape control) of nanopowders has made exploration of a potential metal fuelled engine even more appealing.

If the process is to be examined in the context of recycling the spent metal fuel powder (i.e. oxide) back into metal, then preservation of the nano-structure and size of the original fuel sample upon combustion is critical. It could be argued that the high melting temperature of iron, in conjunction to the fast burning rates and relatively low burning temperatures reported for metallic nanoparticles [2], serve the particular purpose. Moreover, iron oxide reduction to metallic iron is far more straightforward c.f. that of alumina to aluminum and can be readily achieved in one step, e.g. via direct exposure of the spent (oxidized) fuel to hydrogen, suitably produced on-site via renewable means (e.g. solar fuel). Finally, if one also takes into account the substantially higher availability of iron metal (i.e. typical annual production ~20 times larger than that of aluminum), then the potential of nano-iron as a widespread fuel is further enhanced.

Included in this manuscript is work performed on the investigation of nano-iron as a potential fuel for ICE. A similar study for nano-aluminum has already been published [3,4]. To the best knowledge of the authors of this manuscript, there has only been one short publication on iron as a potential ICE fuel [5], which drew some preliminary, yet encouraging conclusions. Recent work has been performed on the combustion effects of adding iron nanoparticles into n-decane or ethanol-based fuels [6] and Diesel [7].

2. Experimental

The reported work involved the study of the oxidation characteristics of four different iron nanopowder. The study implicated powder characterization techniques as well as powder combustion under idealized and non-idealized conditions. Brief description of the experimental equipment is reported below. More information can be found in [3,4].

2.1 Nanopowder characterization

The main difference between the four iron nanopowder grades studied was the average primary particle size (APPS), albeit, as described later in this article, morphological differences were also identified. Two of the nanopowders investigated were purchased from READE Advanced Materials, with designated APPS of 50 nm and 70 nm; these are respectively referred to as Fe50 and Fe70 throughout this article. A third nanopowder grade with a designated APPS of 25 nm was purchased from Nabond Technologies Co. LTD (referred to as Fe25). The fourth nanopowder studied was in-house prepared and had an APPS of 85 nm, as measured by TEM imaging (referred to as Fe85). The preparation of Fe85 involved exposure of iron oxide (hematite/α-Fe_2O_3 with a designated APPS of 20-40 nm/acquired from READE Advanced Materials) in a fixed bed tubular reactor to 100% H_2 flow at 400^oC, followed by cooling to ambient temperature under nitrogen. Subsequently, the obtained product was allowed to settle

inside the reactor for at least 12 hours under ambient conditions to facilitate passivation. Fundamental physicochemical properties of the four nanopowders were obtained by XRD, TEM / Energy Dispersive X-ray analysis (EDS) and specific surface area measurements via the Brunauer–Emmett–Teller (BET) method. Data summarizing all properties measured in-house for the fresh powder samples are shown in 0.

Typical TEM images of the four iron nanopowder types are shown in Figure 1. Size distributions and X-Ray diffraction patterns of the four samples are shown in Figure 2. All samples consisted of dense particles, with the formation of larger agglomerate structures being common. The majority of the particles of the three commercial powder grades were spherical, while those of the in-house built Fe85 had more irregular shaping. The latter was substantiated from BET measurements, where it was found that, contrary to the expected trend on the basis of APPS, Fe85 had a larger specific area (m^2/gr) than Fe50 and Fe70. The TEM images also showed a degree of sintering/aggregation for all powders, particularly so for Fe25 and Fe85. Additionally evident from the TEM images was the fact that all particles were coated by an amorphous oxide layer (Figure 30) of 2-3 nm in thickness, independently of particle size. This layer is generally necessary for the passivation of the individual nanoparticles and its formation constitutes a typical step during their production, in order to avoid undesired spontaneous ignition phenomena upon exposure to ambient air. The presence of atomic oxygen, primarily related to the oxide layer, was verified by EDS analyses of focused TEM images, where average ratios of O/Fe equal to 0.43/0.57 (i.e. corresponding to a stoichiometry close to Fe_3O_4) could be measured along the circumference of some particles. Typical X-Ray Diffraction patterns (Figure 2) for Fe50, Fe70 and Fe85, showed that only the pure metallic phase was detected. In the case of Fe25, the existence of Fe_3O_4 impurities indicated that the oxide phase accounted

for an appreciable amount (i.e. typically in the order of 10 wt% and referring to crystalline phases only). In addition, based on the intensities of the metallic iron peaks of the samples analyzed, Fe25 is clearly the less crystalline one among the four grades. The TEM images of the fresh commercial nanopowders were further analyzed in order to obtain an estimate of the APPS and compare it to the manufacturer's specification. This was deemed as necessary, as the oxidation characteristics of the ultra-fine iron powders investigated were primarily assessed with respect to particle size. It should be noted that the estimation of APPS based on TEM involved the assumption of spherical particles and was performed by tracing the edge of individual particles using imaging software. As it can be seen from 0, a somewhat notable difference between designated APPS and the one estimated from particle-to-particle measurements was identified only for the case of the Fe25 grade (i.e. 25 nm vs. 36 nm). Even so, the differences in terms of APPS for the three commercial nanopowders were clear, hence subsequent correlation between their oxidation behavior and APPS is not jeopardized.

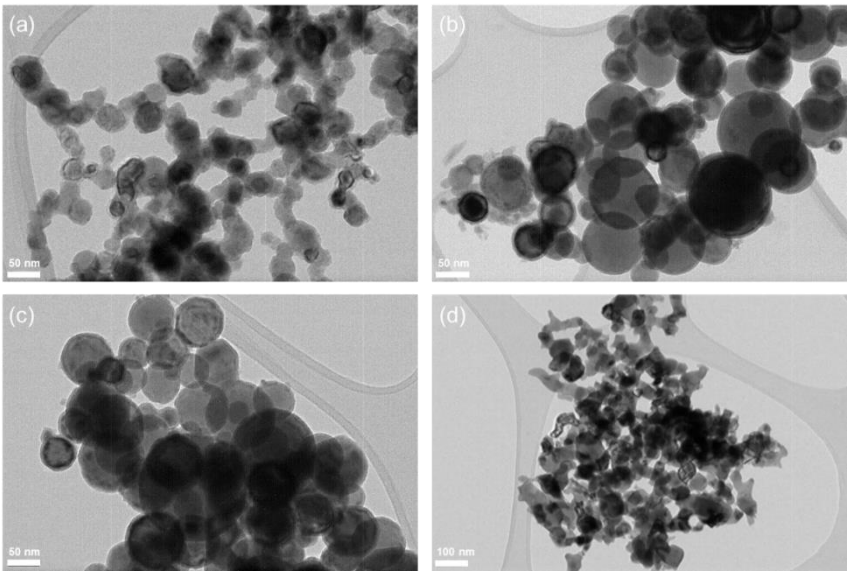

Figure 1. Selected TEM images for fresh powder samples of a) Fe25, b) Fe50, c) Fe70 and d) Fe85

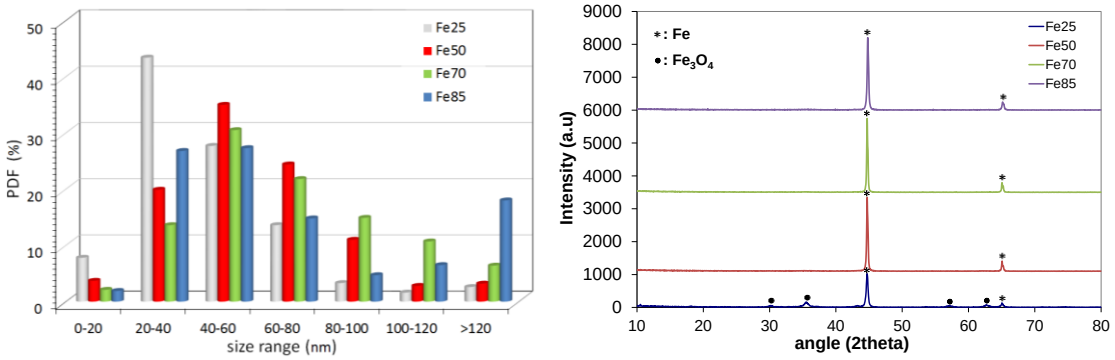

Figure 2. Size distributions (left) and XRD patterns (right) of the four particle samples

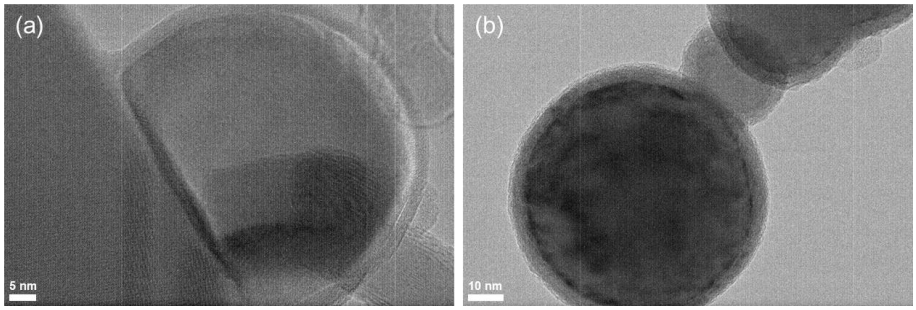

Figure 3. Typical TEM images showing the oxide layer around nanoparticles of the a) Fe25 and b) Fe50 fresh powder samples

Sample Code	Average Primary Particle Size				Average thickness of oxide layer (nm)	BET (m^2/gr)	XRD phases
	Spec. (nm)	APPS from TEM (nm) / No. of particles measured	Size range measured (nm)	Most frequent size range (nm)			
Fe25	25	36 (256)	12-233	20-40 (43.4%)	2-3	26.4	metallic Fe, Fe_3O_4
Fe50	50	59 (234)	16-192	40-60 (35.0%)	2-3	9.3	metallic Fe
Fe70	70	71 (141)	14-190	40-60 (30.5%)	2-3	6.7	metallic Fe
Fe85	NA	85 (216)	13-282	60-80 (25.3%)	2-3	12.7	metallic Fe

Table 1. Measured properties of the four iron nanopowder samples studied.

2.2 Experimental rigs

Evaluation of Fe nanopowder as potential ICE fuel was performed under various conditions. Low temperature oxidation was studied via TGA. High temperature combustion was assessed under idealized (vessel, shock tube) and engine conditions.

The TGA studies of the fresh powders were conducted in a Perkin Elmer Pyris-6 instrument under four different O_2/N_2 environments, with O_2 content ranging between 0% and 100%. The gaseous stream was continuously flowing over the nanopowder container; temperature was increased from ambient conditions to 1273 K by 5 K/min.

Shock tube tests were performed under oxygen-nitrogen mixtures, with O_2 mol fraction ranging from 0.21 (synthetic air) to 0.10, at a pressure of ca. 10 bar and temperatures of 750-1250 K. The apparatus used was of the conventional diaphragm-type, with a running section of 50 mm inner diameter and 6 m long. Helium was used as the driver gas. Typical injection mass was in the order of a few milligrams of powder. The oxidation process of aluminum particles was characterized by means of two-color optical pyrometry. The tests were performed at low particle loadings, with concentrations not exceeding $2x10^{-5}$ g/cm^3. Analysis of the findings was carried out through Planck's law. The wavelengths used were, λ_1=800nm and λ_2=600nm, with a time resolution of 0.4 μs. A schematic of the apparatus can be found in [4].

Details on the constant volume, high-temperature combustion vessel and the methodology followed for the Fe particles combustion visualization have been previously presented in [3, 4]. Basic features of the vessel may include: a) adequate optical access for visualization of the injection/combustion process, b) coil heater for initial temperature control, c) refractory mortar (Greenlite 45 L) for insulation and consequent minimization of heat losses through the walls and d) batch operation, pressurized gas stream powder injection system. A shadowgraph arrangement was used for combustion imaging. Images were recorded at a rate of 21000 fps, with an exposure time of 4.4 μs and resolution of 960x320 pixels, via a Phantom V12.0 camera.

Engine tests were performed in an air-cooled, 350cc single cylinder compression-ignition engine, with a compression ratio of 20.3. The overall engine rig incorporated

an intake air conditioning system (heating, filtering, damping), an exhaust conditioning and sampling system (diesel particulate filter, gas analyzer) [4] and a customized system for direct injection of controllable quantities of powder inside the cylinder (Figure 4). A National Instruments data acquisition system was employed for recording of the intake, cylinder and exhaust temperatures and pressures. The injection system comprised a nanopowder reservoir placed upstream a unidirectional poppet valve and downstream three electro-pneumatic valves (Figure 4). Pressurized air (8 bar) was used as the carrier gas. The system permitted one combustion cycle per test, as the powder reservoir had to be refilled after each injection. Injection was synchronized with intake valve opening. Compared to the original engine configuration, the large orifice of the one-way check valve of the injection system led to an increased clearance volume and thus the reduction of the volumetric compression ratio, from 20.3 to 14.0.

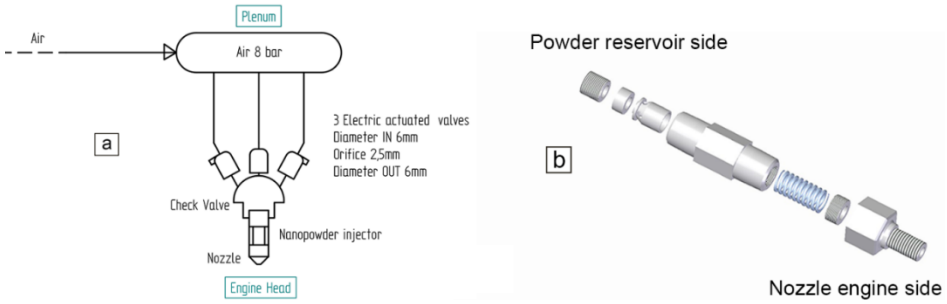

Figure 4. Schematic of the customized direct injection system

The performance of the injection system was analyzed by means of visualization of the powder dispersion in a transparent vessel at atmospheric pressure. A high speed camera (Redlake Motion Scope PCI) was used, having image resolution of 480x420x8bit pixels per frame and recording rate of 8000 frames per second (fps). A Canon TV Zoom lens (V6x16–16÷100mm–1.9 Macro) was coupled to the camera.

A set of combustion runs were performed with the injection system of Figure 4 (i.e. direct injection of nanopowder inside the cylinder). In a second set of engine runs, the

engine head was further modified to allow luminosity emission measurements of the burning particles. To this respect, the injector was replaced with an optical probe placed on the engine head through a quartz window and linked with the two-color pyrometry setup used during tests in the shock tube. The intake manifold was accordingly machined in order to accommodate the customized injector just upstream the intake valve, thereby emulating a Port Fuel Injection system (PFI).

3. Results and Discussion

3.1. TGA study

The TGA experiments examined the reaction temperature profiles of Fe particles of various sizes under different N_2/O_2 atmospheres. Given the fact that iron nitridation is thermodynamically unfavorable under the conditions employed [**¡Error! No se encuentra el origen de la referencia.**3], only the oxidation reaction was considered. All TGA experiments were performed at a heating rate of 5 K/min for temperatures of up to 1273 K. Displayed in Figure 5 are TGA profiles for the standard Fe nanopowders investigated during the currently reported study as well as for a coarse, micron-sized Fe powder, which has been included for direct comparison purposes (i.e. nano- vs. micron-sized particles oxidation behavior).

In comparison to the nanopowders examined, the maximum conversion rate (i.e. highest slope of TGA curve) for the micron-sized sample was shifted to noticeably higher temperatures, in the range of 700-800 K. Maximum conversion rate for the nanopowder grades occurred at approximately 500-600 K, while a conversion ratio of at least 90% had been achieved at T = 650 K, which is similar to findings reported in [14] for TGA of iron nanoparticles of 45 – 400 nm under air. With the exception of a clear trend between Fe50 and Fe70, an apparent correlation between conversion rate and the APPS of the nanopowders examined could not be readily identified. Arguably,

the in-house prepared Fe85 grade was the most reactive powder studied under TGA. This could be related to the relatively irregular shape of the Fe85 particles which allowed for a larger area of contact with the surrounding gas in comparison to that of the almost spherical Fe25, Fe50 and Fe70 nanopowders (as previously shown in Figure 1). The above is also supported by the BET analysis data in Table 1.

Values for total weight gain during TGA in air (Figure 5a) were typically measured to be similar to the theoretical values estimated by assuming a) full oxidation into Fe_2O_3, b) spherical particles and c) fresh sample passivation layer of 2 nm in thickness (Table 1). Significant discrepancy between measured and estimated weight gain was found only in the case of Fe25 (20.6% c.f. 29.5%). This was, to an extent, justifiable via the XRD results already displayed in Figure 2, which revealed that Fe25 was the only nanopowder containing impurities of Fe_3O_4 (and was therefore already partially oxidized) in its fresh state. Arguably, factors such as primary particles morphology and nanopowder composition are also of prime importance and may actually alter the established trend of increase in particle reactivity with decrease in APPS.

Results for the effect of oxygen content on powder reactivity are displayed in Figure 5b. Note that although these results refer solely to Fe85, the behavior of the remaining Fe nanopowders was largely similar. Naturally, increasing %vol in O_2 from 2% to 100%, accelerated oxidation. However, no notable differences were identified between synthetic air and pure O_2 environments. The TGA performed in pure N_2 for temperatures up to 1273 K revealed very low conversion rates. The weight gain for Fe85 was measured at a maximum of 2.9% by 1273 K. Since nitridation of Fe is highly unlikely under the conditions employed, this weight increase was ascribed to limited leakage of ambient air introduced into the sample environment.

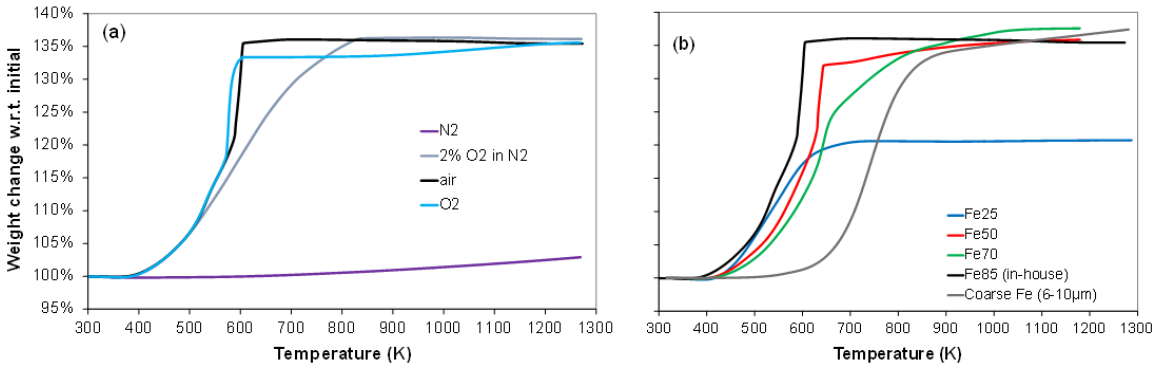

Figure 5. TGA analysis under air for the nanopowders studied as well as for a micron-sized iron powder (a) and under different atmospheres for Fe85 (b).

3.2 Shock-tube study

Shown in Figure 6 is the time evolution of the thermal radiation and temperature signals for Fe85 nanopowder burning in synthetic air. The results shown refer to data from typical tests with estimated ignition temperatures of as low as 600K. Time zero corresponds to the arrival of the incident shock in the measurement section, whilst the dotted line in each plot corresponds to the reflected shock.

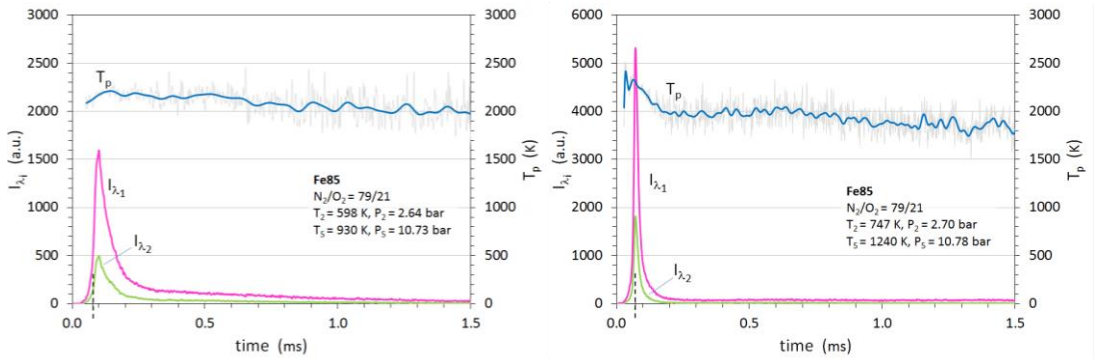

Figure 6. Thermal radiation signals and temperature for Fe85 burning in air. The terms T_2, P_2 and T_5, P_5 refer to the incident and reflected shock conditions respectively.

The particles exhibited rapid ignition, as evidenced by the abrupt increase of the thermal radiation signal. As reaction proceeded, the thermal radiation signal decreased, indicating the combustion boundaries and corresponding burning time. Most tests

performed with Fe85 revealed a distinctive behavior with a slower combustion event following the initial combustion phase. This could be attributed to the presence of a significant fraction of particles larger than 120 nm in the Fe85 sample (see Figure 2). Arguably, the initial rapid increase in $I_{\lambda 1}$ reflected burning of the smaller particles, whereas the residual $I_{\lambda 1}$ signal following indicated burning of the larger particles.

Peak temperatures measured (ca. 2200-2300 K) were above the melting points of Fe and its oxides (FeO, Fe_2O_3, Fe_3O_4) [15], but comfortably below their boiling and/or dissociation temperatures at the pressure range investigated [16]. Hence, particle material evaporation is highly unlikely to occur during the combustion phenomenon. It could thus be argued that oxidation proceeds heterogeneously [1] on the surface of particles. The pyrometry measurements suggested intense combustion during which particles melt and the main intermediate products are likely FeO and Fe_3O_4, since Fe_2O_3 cannot exist (decomposes) above 1735 K. As the temperature of the particles drops, it is thought that particles complete their oxidation process towards Fe_2O_3, as implied by TEM post-analysis of combusted particles. Having excluded evaporation and dissociation effects, the temperature rise because of oxidation is solely limited by the heat transfer through conduction to the ambient gas and radiation to the walls of the shock tube. It is worthwhile to remark that the average particle size is comparable or smaller to the gas mean free path, with Knudsen numbers close to or slightly above unity, where the continuum particle-gas interaction regime ceases being realistic. In this case, particle combustion is presumably kinetically-controlled [17]. Thorough description of heat transfer processes relevant to nanoparticles can be found in [18].

The effect of O_2 concentration on the combustion of Fe85 nanoparticles can be evident via comparison of the results of Figure 7, with O_2 concentration of 21%, to those of Figure 80 obtained for O_2 concentration of 10%. The net effect appears to be a

noticeable slowdown of the process and a decrease of the combustion temperature from 2300 K to 2000 K. It should be noticed, that the characteristic pattern of an initial abrupt combustion phase, followed by a second much slower combustion stage, remained.

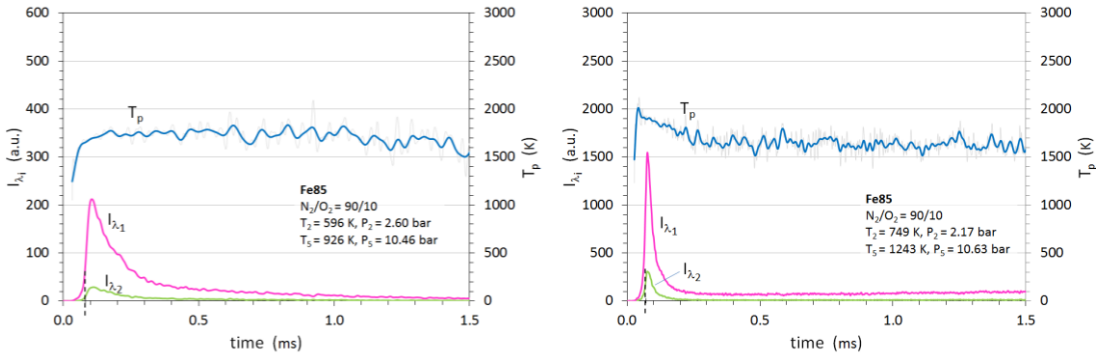

Figure 7. Thermal radiation and temperature for Fe85 burning in 90% N_2 - 10% O_2

Shown in Figure 8 (left) below are the normalized signals of the thermal radiation at 800 nm for Fe85 nanopowder burning in synthetic air. The results provide an overall picture of the combustion behavior of the nanopowder at different atmospheres and/or reflected shock temperatures (T_5). Corresponding burning times are included in Figure 8 (right). The burning time (t_b) values were estimated to be equal to the time interval measured from the point of onset of the incident shock in the measurement section (dotted lines in Figures 7 and 8) to the point where the main combustion phase ceases, as evident by the apparent decrease in the slope of the I_{800} ($I_{\lambda 1}$) vs time curve. As expected, the higher the reflected shock temperature the shorter the burning time.

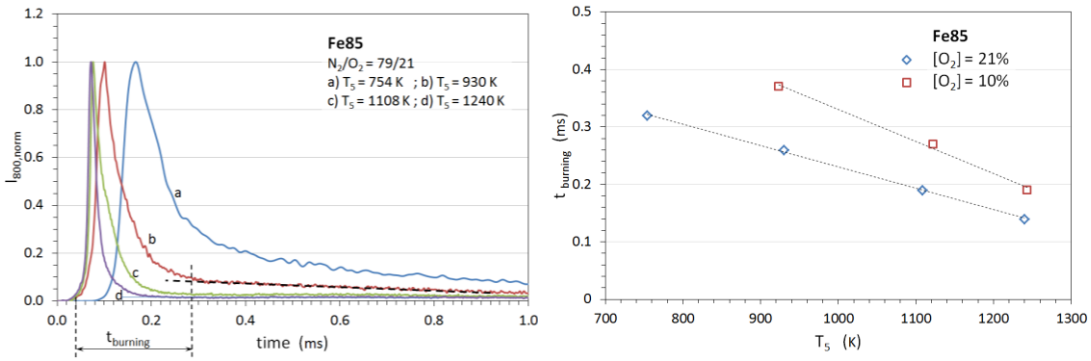

Figure 8. Left - Thermal radiation at 800 nm for Fe85 nanoparticles burning in synthetic

air at four different reflected shock temperatures. Right - Duration of the main combustion phase for Fe85 nanopowders burning at two different atmospheres.

Sample results for Fe50 nanopowder are shown in Figure 9. The pyrometry signals show that the burning time encapsulated most of the combustion event, as confirmed by the sudden drop in measured temperature. The Fe50 nanopowder grade was less reactive than Fe85 and they hardly ignited below 800 K in air. Results for the average burning time of Fe50 at various reflected shock temperatures are displayed in Figure 10. The immediate observation is that, at given initial conditions, burning times for the main combustion phase of the Fe50 powder are longer than those for Fe85.

Although the shock tube and TGA environments are considerably different (conditions, powder dispersion and consequent bulk diffusion and kinetics), findings with respect to overall nanopowder performance were consistent between the two techniques, with Fe85 being more reactive than Fe50. As already explained during discussion of the TGA results, the morphology of Fe85 resulted to higher average particle surface area compared to that of Fe50 (supported by the BET measurements of Table 1). The established inversely proportional correlation between nanoparticle size and reactivity is predominantly surface area driven. Since particle size and mean free path are comparable, the continuum burning model is not valid and oxidation is likely more of a surface process involving the collision of oxygen with the particles and then the subsequent transport through the oxide shell [19]. The above agree to the increased reactivity of Fe85 compared to Fe50, as evidenced in the shock tube results. It is reasoned that in the case of the shock tube study there could be a further occurrence ultimately contributing to the observed behavior. From the TEM originated PSDs the Fe85 grade exhibited a particle size distribution of a more polydisperse nature compared to the other particle grades, with two distinct modes at d_p = 20-60 nm and d_p > 120nm.

Albeit closer inspection of the TEM images for the fresh samples suggest more prominent aggregation (sintered clusters) for Fe85 compared to the other grades studied, the presence of large agglomerates cannot be dismissed. Strongly sintered aggregates require substantial energy for segmentation, however, the severity of the reflected shock could in fact break-up large agglomerates or weakly formed aggregates [20]. This holds for all powder grades, but based on the TEM derived PSDs, such effects would statistically be more important for Fe85, yielding an APPS at the start of combustion of notably less than 85 nm and consequently even larger average surface area (and reactivity) for Fe85 c.f. for Fe50.

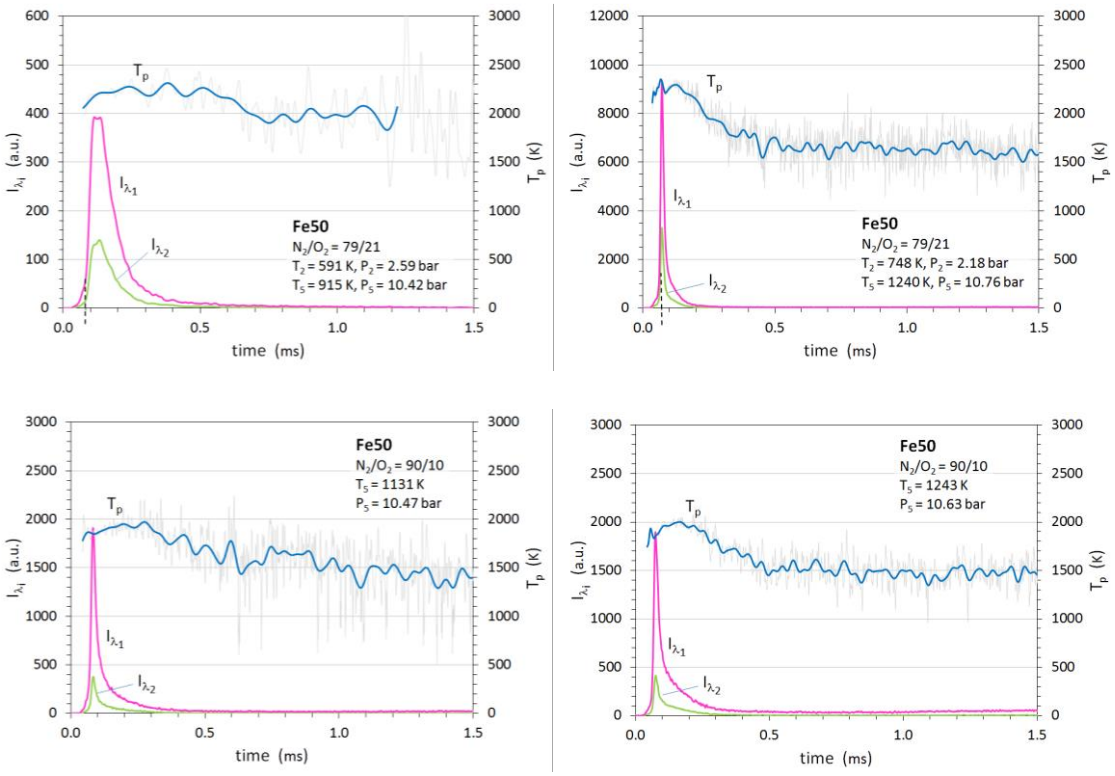

Figure 9. Thermal radiation and temperature for Fe50 burning in synthetic air.

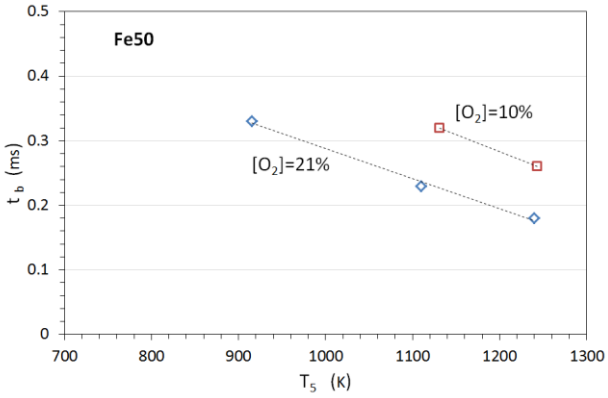

Figure 10. Burning times of Fe50 nanopowders in synthetic air and with 10% of oxygen.

The aforementioned correlation between nanopowder reactivity and surface area requires further investigation in order to draw more quantitative results via repetition of the shock tube tests for more powder grades. Arguably, a significant overall conclusion from the shock tube results is the fact that the burning times of the nanoparticles were found to be inversely proportional to the square root of oxygen content. In accordance to literature [19], it could be argued that the rate-limiting step of the metal nanoparticles combustion is the dissociative adsorption of the oxygen molecules at the gas/oxide interface. A sticking coefficient is generally defined as the adsorbed fraction of the oxygen molecules hitting the particles surface. This coefficient depends on the particle temperature and on the energy and orientation of the hitting molecules, as suggested by the dependence of the burning time from the gas temperature. Presumably, the chemisorbed oxygen atoms then react with the Fe cations which fast diffuse outward through the oxide layer.

Analysis of the burned particles with TEM (Figure 11) disclosed evidence of sintering. The level of particles sintering was higher for the low oxygen concentration employed (Figure 11b). Depth of oxidation depends on the particle size, the maximum particle burning temperature and the cooling rate. As the oxide thickness grows, the surface available (internal oxide/metal interface) for the migration of Fe cations decreases as

well. If particles cool and start to solidify, any diffusive process drastically decreases and particles ‘‘freeze’’ in a state of partial oxidation (dominant in Figure 11b. The irregular shape of the surface of partially oxidized particles could be ascribed to differences in the thermo-physical properties of iron and its oxides (melting temperatures, viscosity, and surface tension). On the contrary fully oxidized particles (dominant in Figure 11a) appeared spherical with smoother surface. The presence of a large number of spherical fully oxidized particles (Figure 11a) suggests a liquefaction and re-solidification process that occurred extensively during the main combustion phase. Following their full oxidation and shortly after temperature dropped below their melting point, the iron oxide droplets obtained their near spherical shape. Such a claim is also supported by the fact that, as depicted in Figure 1d, fresh Fe85 particles were of irregular shape and extensively aggregated. It is also noted that the complete oxidation of such particles was confirmed via EDS analysis, which revealed an O/Fe atomic ratio very close to 1.5, thereby corresponding to the Fe_2O_3 state.

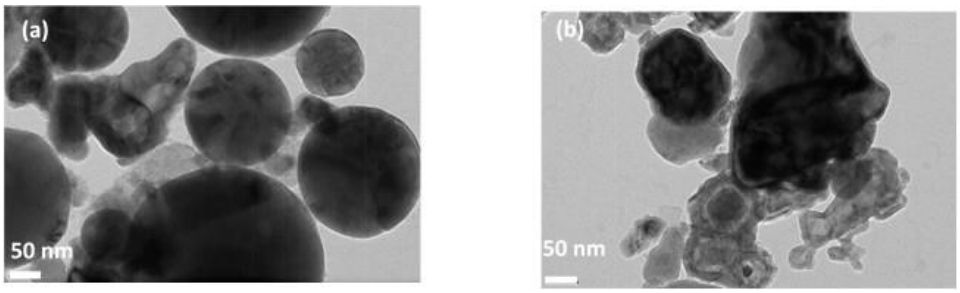

Figure 11. Representative TEM images of Fe85 particles after oxidation under shock-tube conditions: a) sample combusted in air and T5 = 1243 K, b) sample combusted in N2/O2 = 90/10 mixture and T5 = 1240 K

3.3 Combustion vessel study

Tests were conducted for different Fe nanoparticle grades, Fe25, Fe50 and Fe85 at an initial temperature of 973K and two different initial pressures of 10 bar. The amount of

fuel injected was 30 mg for all runs. The combustion process evolution is described via the plots of Figure 12, including in-vessel pressure increase and light intensity at the photodiode at the two different initial pressure values explored. In overall consistency to the TGA and shock tube results, Fe85 burned faster (evident from $\Delta P/\Delta t$) compared to Fe50 and Fe25 at both initial pressures examined. Similar trends were also revealed from the luminosity results as well as the results from sample flame images obtained with the high speed camera at t = 4.0 ms after ignition (Figure 13). Reasoning behind the observed behaviour remains as discussed above for the TGA and shock tube results.

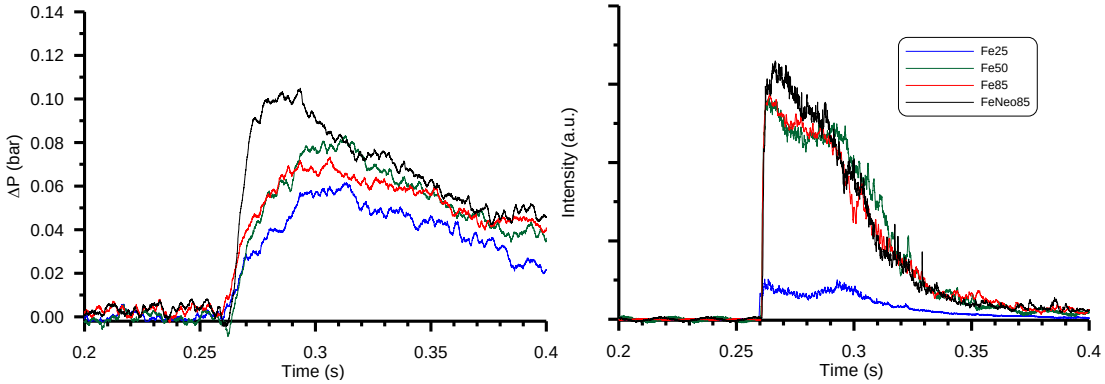

Figure 12. Pressure increase in the combustion process (left) and flame luminosity (right) for Fe25, Fe50 and Fe85. 30mg injected, P = 10bar, T = 973K

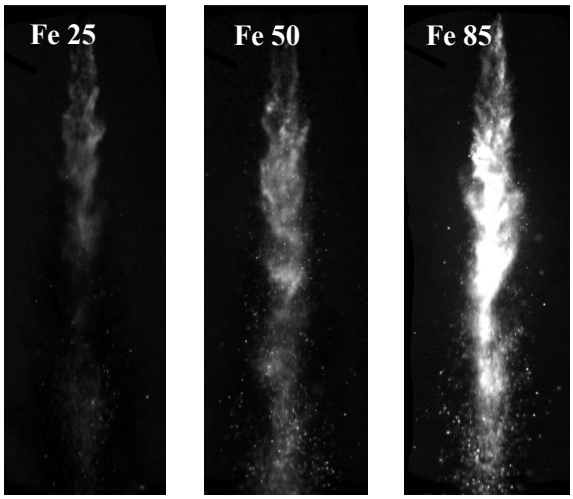

Figure 13. Images of combustion process for three different types of Fe nanoparticles (Fe25, Fe50, Fe85). 30mg injected, P = 10bar, T = 973K

The images of Figure 13 allow for an overall visual inspection; nonetheless to facilitate a better comparison between the different grades of Fe nanoparticles, a data reduction procedure was developed to represent the flame evolution on the basis of accumulated light intensity from imaging analysis over the whole event. These results are summarized in Figure 14 for all experimental conditions (i.e. particle grade, initial pressure). Time data in the plots are referenced (t = 0) with respect to the time of observation of the first particles in the recorded images. Ignition delay, defined as the time between t = 0 to time when first particles were illuminated, was found to be similar (10-12 ms) at all tested conditions. Nonetheless, the image-derived light intensity results unsurprisingly followed the trend of the pressure-time and photodiode results, with Fe85 yielding the highest light intensity, trailed by Fe50 and Fe25.

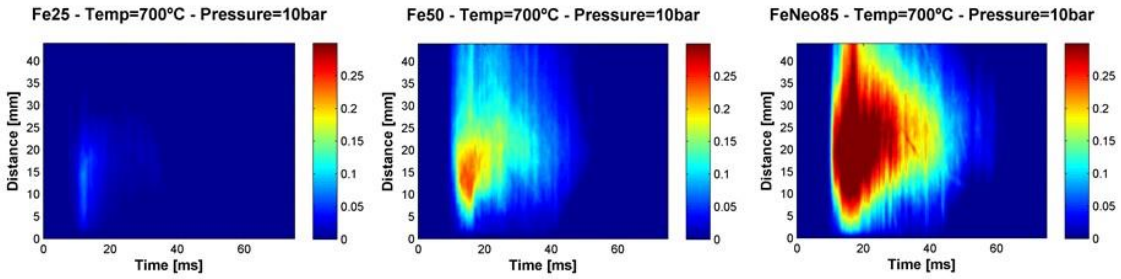

Figure 14. Normalized accumulated light intensity of combustion process for three different types of Fe nanoparticles. 30mg injected, P = 10bar and T = 973K

3.4 Engine study

Considering the proof of principle nature of these experiments, engine tests were performed for the Fe85 grade only, as this was the arguably the most reactive powder grade as emerged from the TGA, vessel and shock tube studies presented earlier.

Preliminary tests under motored conditions indicated that an engine speed of 1500 RPM would offer the best compromise between stable engine running conditions (i.e. without

excessive torsional stress in the driveline) and adequate time during the intake and compression strokes (40 ms in total) for the injection of powder.

The performance of the injection system was preliminarily assessed by means of high-speed visualization of powder dispersion in a transparent vessel at ambient pressure. The tests were performed varying the injector pulse width (IPW), namely the opening time of the electrovalves, at different powder loadings from 50 mg to 200 mg, using the Fe85 nanopowder grade. The pressure of the carrier gas was 8 bar throughout the tests. After each test, the injector reservoir was checked for any powder residue. Figure 15 shows a sequence of images relative to the injection of 100 mg of powder. The frame rate was 2000 fps. A compact jet emerging from the nozzle tip can be observed at about 13 ms after the start of excitation of the injector (ASOEI), with the injection process practically lasting 13-14 ms. Upon increasing the powder loading to 200 mg, the actual injection duration increased to circa 22ms, while the injection delay remained practically unchanged at 13 ms.

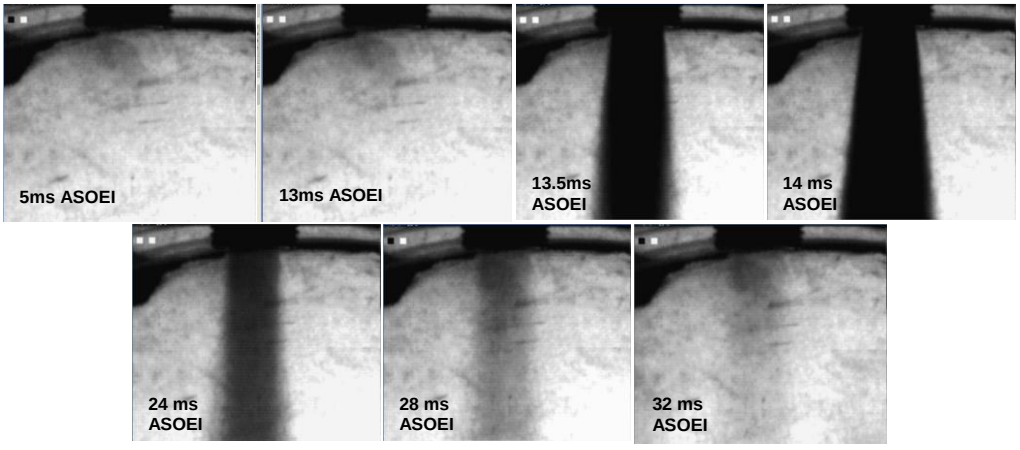

Figure 15. Frame sequence (2000 fps) of the injection of 100mg of Fe85 powders, at an injection pressure of 8bar.

Based on the above findings, it was determined that for an engine speed of 1500 RPM, the injection system was suitable to provide up to 200mg of powder in a timeframe

from the start of the intake stroke up to approximately 50 crank angle (CA) degrees Before Top Dead Center (BTDC) (i.e. a total window of 310 degrees in CA or 34.4 ms at 1500 RPM). The injection window was limited to 50 CA-BTDC because of the increasing back pressure during the compression stroke.

Engine combustion runs with direct injection of the powder inside the cylinder (injector placed at the center of the cylinder head) were performed with powder quantities of 50 mg to 200 g. For each powder charge, several identical tests were conducted for repeatability assessment purposes. Nevertheless, for powder charges of 50 – 100 mg the combustion was generally too weak, resulting in marginally detectable increase of the in-cylinder pressure. Tests with 200 mg of powder charge showed significant evidence of particle combustion. In this case, the nominal fuel excess ratio was equal to 0.7 (corresponding to a lean overall fuel-air charge). Therefore, several test runs, with more than 15 single shot injections each, were performed. Displayed in Figure 16 are typical results showing the evolution of the cylinder pressure trace of the first series of runs, from test number 1 to 10, with injected powder mass of 200mg of Fe85 and start of actual injection at 250 CA degrees BTDC; the motored-engine pressure (dotted line) and the injection timing window are also shown. Fine combustion was observed during the first four cycles, raising the cylinder pressure up to ca. 75 bar. However, fouling of the one-way check valve of the injector and its progressive clogging degraded the injector operation, leading to progressive decrease in the combustion pressure for the later test runs, with test 10 yielding a peak pressure of 45 bar (i.e. 40% reduction c.f. cycle 1). In fact, cleaning the check valve upon completion of the run and then re-running the engine resulted to temporary restoration of the peak pressures at values of ca. 75 bar. It could be reasoned that the clogging problems encountered are of a technological nature and could be overcome via implementation of a more complex and

rigorously designed system. Nevertheless, the fact that the first few cycles of each run clearly provided combustion traces at high peak pressure, and with good repeatability, is quite encouraging. Even for the later cycles, where clogging of the injection system had occurred, a notable increase in pressure early in the compression stroke was observed, indicating the occurrence of combustion in all cases.

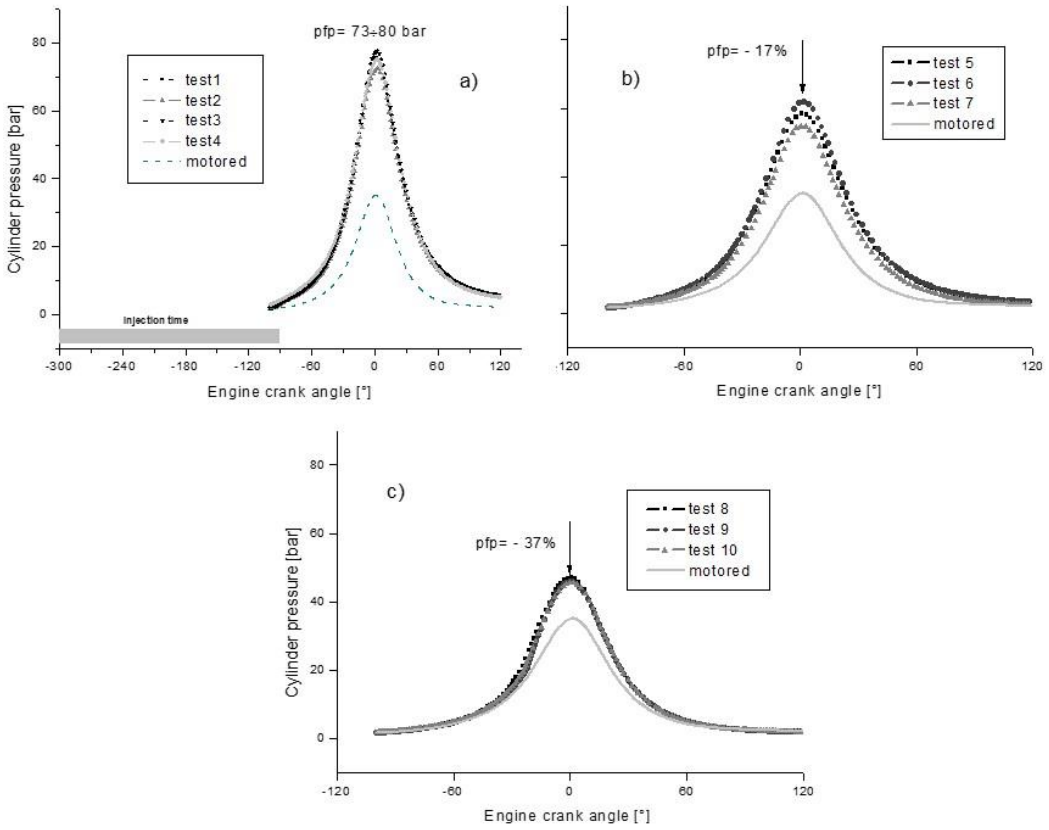

Figure 16. In-cylinder pressure evolution for different combustion tests at 1500 rpm and 200mg of injected powder mass of Fe85. Shown in plot (a) is the injector energizing time (25ms) and the effective injection duration (13ms) for carrier air pressure of 8 bar.

A thermodynamic analysis of the cycles 1, 2 and 4 was carried out inferring the mean gas temperature, the apparent heat release (HR) and the apparent rate of heat release (ROHR) [21]. Respective results are shown in Figure 17. It is worth noting that the estimated heat release reported in Figure 17d represents the heat exchange process between particles and cylinder gas only, while the heat loss through the wall is not

considered. It can be observed that particles started to burn at about 100 CA-BTDC, as the compressed gas temperature reached 500 K. This observation is in line with relevant iron nanoparticles combustion data previously reported [5]. Moreover, the peak thermodynamic gas temperature was calculated at around 1500-1600 K. Based on the curves of heat release and heat release rate, combustion of iron nanoparticles appeared to develop in two distinct phases, a behavior that has been reported in previous published work [3]. A rapid heat release was observed immediately after ignition, suggesting a fast oxidation process of the iron nanoparticles [19]. The ROHR peaked around 1ms after ignition, prior to decreasing back to values close to zero. A second HR phase started around 90 CA later (i.e. close to TDC). Here, more energy was released c.f. the first phase of HR, however this occurred according to a more progressive pattern, thereby suggesting slower reaction rates. The total combustion duration was about 220 CA, with the first phase lasting for about 7-8 ms whereas the second phase lasted for 13-15 ms. This corresponded to about 4 times longer combustion time than that of a typical diesel engine. It can be recognized that this relatively long duration of combustion limited the thermal efficiency of the engine. Furthermore, as particles ignited at about 100 CA BTDC, a significant fraction of heat was released during the compression stroke, thus increasing the pumping work of the engine, as shown in Figure 18, where the cylinder pressure history and normalized cylinder volume is plotted together with the relative pumping work and high and net indicated mean effective pressures (IMEP). This behavior was strictly inherent to the injector operation and its long opening times. As previously stated, the customized injector used was able to inject 200 mg of fuel in approximately 22 ms. This was almost one order of magnitude longer than the typical injection duration for a CI engine running on diesel (as low as 2-3 ms at 1500 RPM). Pumping losses could be

substantially reduced if the particles were closer to TDC and with shorter injection times, however the net IMEP determined was still within the same order of magnitude to that of a typical CI engine running on diesel fuel.

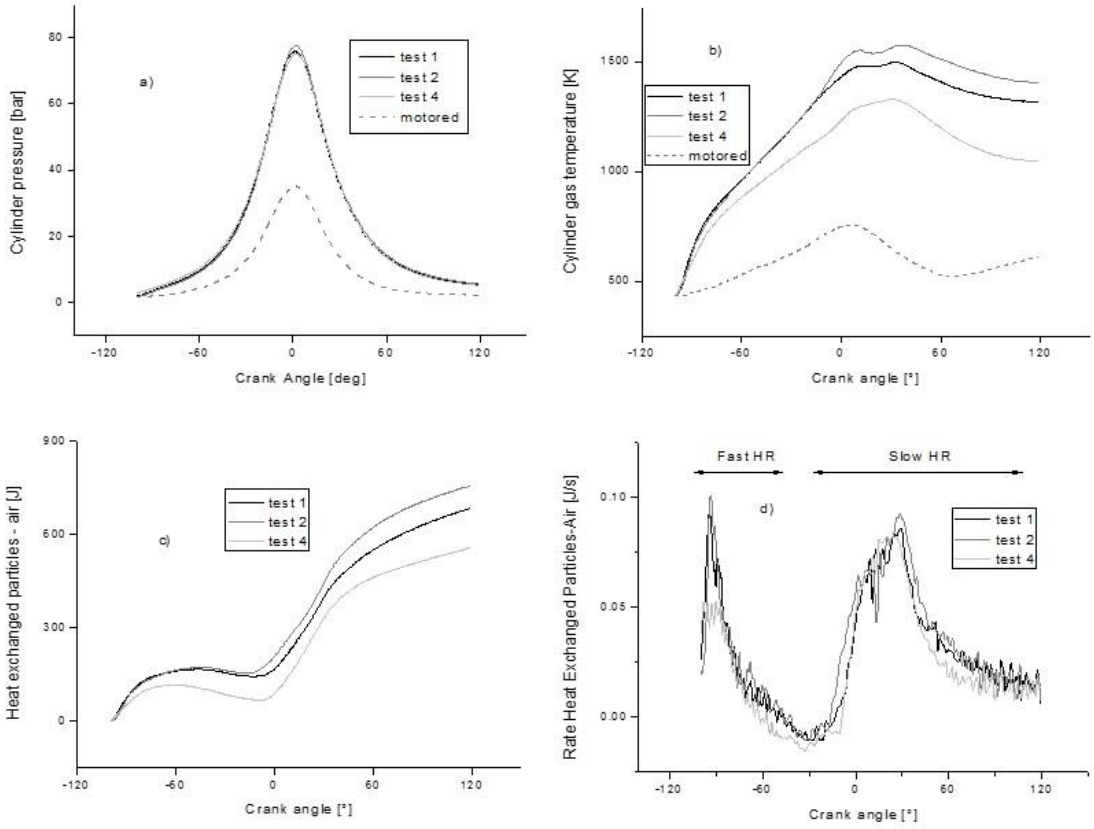

Figure 17: Pressure (a), temperature (b), heat release from particle combustion (c) and rate of heat release (d) versus engine CA for tests with 200 mg of Fe85 injected

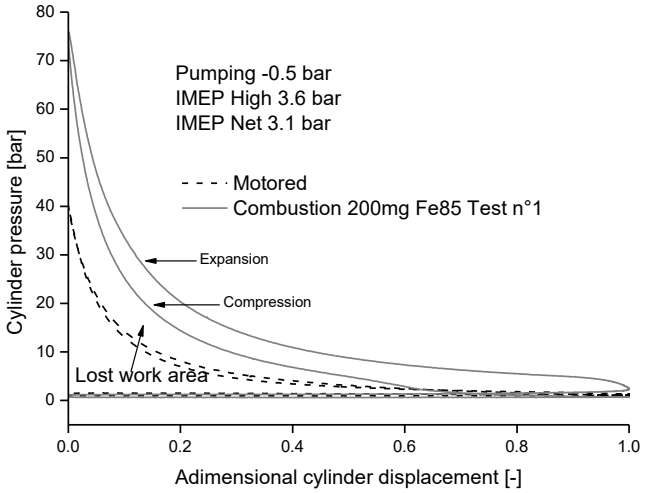

Figure 18 – Pressure plotted against normalized cylinder volume

Additional engine combustion runs were carried out with the injector system moved upstream the intake valve to enable measurements of particle luminosity emission. Rate of heat release, luminosity emissions and gas and particle temperatures for a sample cycle with 200 mg of powder injected are shown in Figure 19. It should be noted that in this case there was an additional delay in ignition time and consequently combustion started at a slightly higher cylinder temperature (ca. 600K). The ROHR and luminosity results of Figure 19 suggested that large part of radiation was emitted during the initial, fast combustion phase (from 30 to 10 CA degrees BTDC). For the second combustion phase (starting at around TDC), even though there was substantial HR, the luminosity signals were below the sensitivity threshold of the detectors. The average particle temperature attained maximum values of around 2200 K just before the ROHR peak during the initial combustion phase, with a subsequent cooling phase. The difference between average particle temperature and gas temperature was found to be as much as 1000 K at 20 CA degrees BTDC. This difference was similar to that observed for a typical diesel combustion case between soot particles and the surrounding gas [22].

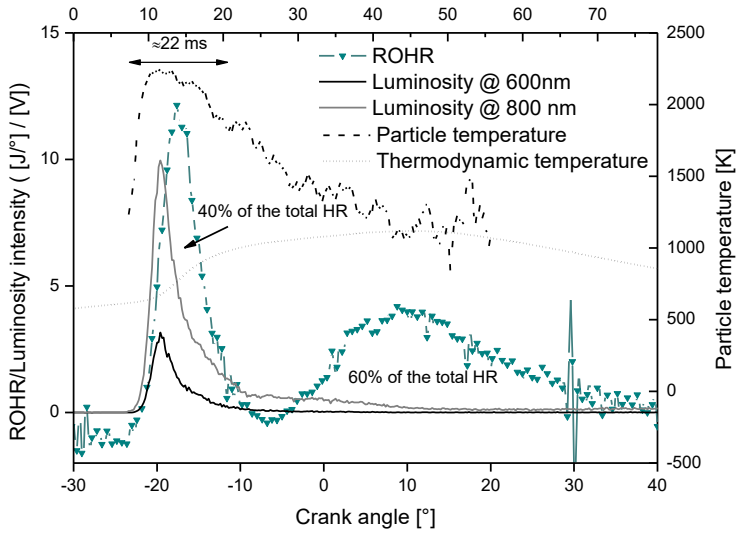

Figure 19. Rate of heat release, luminosity emissions and gas and particle temperatures for a sample cycle with 200 mg of powder injected

Considering the engine results displayed above and also based on descriptions of metal nanoparticle oxidation reported in the literature [2, 5, 17, 19, 23], combustion of iron nanoparticles in a CI engine could be speculated to be as follows. Following particle heating up during the compression stroke, combustion starts when the thermodynamic temperature reaches ~500-600 K (on the basis of apparent pressure increase w.r.t. motoring conditions). Once ignited, the particles quickly attain their maximum temperature close to 2200 K. This is primarily caused via interaction of the oxygen present around and within the external layer of the particles and Fe in the particles core. Due to the high surface/volume ratio of the primary particles, this phase corresponds to the highest oxidation rate and hence maximum combustion temperatures are reached. Considering that the high temperature of the particles (~2200k) melting of either the iron (1808 K) or the Fe oxides (1650 K for FeO, 1811 K for Fe_3O_4, 1820 K for Fe_2O_3) present in the system at this stage is highly possible. This could also justify the observed sintering of the external layer of the spent particles (Figure 20a). On the other hand, appreciable volatilization of the metal or oxide in the surrounding gas could be safely ruled out (both > 3000 K). Following the initial surface oxidation phase, the process then proceeds toward the inner core of the nanoparticles and the oxidation rate becomes limited by the oxygen diffusion rate within the particle core. In engine terms, this phase occurs slightly after the TDC, where thermodynamic cooling of the bulk gas and hence the particles starts to occur. Here, two potential processes are thought to govern the slower heat release rate calculated from the experimental data. A slow oxidation driven by the oxygen diffusion in the inner core of the particles or a phase change (solidification) of liquified particles. Independently of the route followed, experimental evidence suggests that at 40-60 CA degrees ATDC, the gas expansion stops the

combustion. It is expected that metal and/or the oxide liquefaction should lead to higher combustion rates, as observed in [4] for engine combustion of aluminum nanoparticles. Further studies on iron nanopowder combustion are required to bolster the overall mechanism suggested above. However, first evidence confirming the above claims were provided by TEM post analysis of particles collected downstream of the engine. Figure 20 depicts two indicative such images. Figure 20a shows a typical highly aggregated structure, thereby revealing the occurrence of fusion of several neighboring primary particles (please refer to Figure 1d for direct comparison) during combustion. EDS analysis of several such structures revealed O/Fe atomic ratios in the range of 1.0-1.2. Thus, taking into account the stoichiometry of fully oxidized Fe_2O_3, overall combustion was only partial. The higher resolution image in Figure 20b clearly shows a thick oxide shell of approximately 30 nm (c.f. the 2-3 nm thick oxide shell of fresh metallic primary particles), in which an iron core is encapsulated.

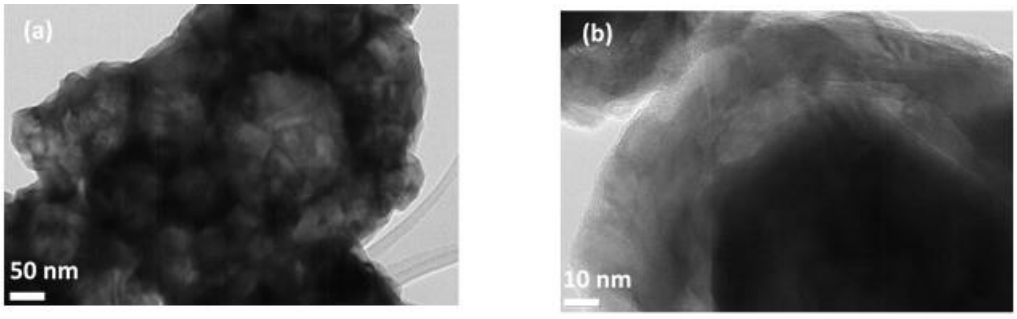

Figure 20. Indicative TEM images of combusted Fe85 particles collected downstream of the engine

Regarding the energy balance of the process, partial particle oxidation as well as the unfavorable timing of the heat release with respect to the expansion stroke appears to limit the effective energy harnessed. It is therefore important that future studies would exploit a combustion system with higher oxygen concentrations and employ a more

suitable injection system able to inject metal fuel at a faster rate and ensure clogging-free operation over a substantially higher number of combustion cycles.

4. Conclusions

A study was conducted in order to examine the proof-of-principle feasibility of iron nanopowder combustion and its characteristics under idealised and engine like conditions. Several nanopowder grades were examined, primarily differing in average particle size and, secondarily, morphology. Several rigs were employed, including TGA, shock tube, combustion vessel and a single cylinder experimental engine.

The TGA measurements showed that, overall, the weight gain due to oxidation of the nanopowders was close to that for full oxidation of spherical particles into Fe2O3. However, it was generally highlighted that factors such as average particle morphology and nanopowder composition were also of prime importance and could actually alter the established trend of increase in particle reactivity with decrease in APPS. For instance, the relatively more irregularly shaped Fe85 had a higher surface area compared to the more spherical Fe50, and was consequently found to be more reactive. No notable differences in TGA oxidation characteristics were identified between synthetic air and pure oxygen environments.

Peak temperatures measured in the shock tube experiments were above the melting points of Fe and its oxides, but securely below the respective dissociation temperatures. Particle evaporation was thus prevented and, arguably, oxidation proceeded heterogeneously on the surface of the particles. Shock tube results revealed similar trends similar to those observed in TGA, with the surface area being again identified as the most important factor in controlling powder reactivity. This could be reasoned by considering that, since particle size and mean free path were comparable, oxidation likely proceeded outside the continuum burning model and was thus more of a surface

process involving the collision of oxygen with the particles and then the subsequent transport through the oxide shell. Nonetheless, a degree of the observed behaviour could also be attributed to the different levels of polydispersity of the different powder grades. The higher reactivity of the Fe85 c.f. Fe50 and Fe25 particles was also verified via the combustion vessel studies, as suggested by recordings of $\Delta P/\Delta t$ as well as particle luminosity and light intensity. No notable discrepancies were found in terms of ignition delay between the different particle grades.

Engine tests were performed solely for Fe85 particles and, albeit clogging problems were encountered with the injection system, largely confirmed the feasibility of Fe nanoparticle combustion in a lightly modified CI engine. For a nominal engine compression ratio of 20.3, peak pressures encountered were in the range of 70-80 bar. Peak thermodynamic gas temperatures were determined to be around 1500-1600 K, with maximum particle temperatures estimated to be as much as 1000K higher at around 20 CA degrees BTDC. Estimates of net IMEP were found to be within the same order of magnitude to those of a typical CI engine running on diesel fuel, at approximately 3.1 bar. TEM imaging analysis of combusted particles revealed a level of sintering, while EDS analysis suggested partial oxidation of particles.

Acknowledgements

The authors would like to thank the European Commission for partially funding of this work through the Project “COMETNANO” (FP7-NMP4-SL-2009-229063).

References

1. Glassman I., Yetter R.A., Combustion, 4th ed., Academic Press, 2008, ISBN 978-0-12-088573-2

2. Yetter R.A., Risha G.A., Son S.F., Metal particle combustion and nanotechnology. Proc Comb Inst, 2009, 32, 1819-1838

3. Karagiannakis G., Mandilas C., Konstandopoulos A.G., Beatrice C., Lazzaro M., Rispoli N., Pastor J.V., Ros E., Molina S., Determination of oxidation characteristics and studies on the feasibility of metallic nanoparticles combustion under ICE-like conditions. SAE Int J Fuel Lubr, 2011, 4, 282-297

4. Mandilas C., Karagiannakis G., Konstandopoulos A.G., Beatrice C., Lazzaro M., Di Blasio G., Molina S., Pastor J.V., Gil A., Study of Basic Oxidation and Combustion Characteristics of Aluminum Nanoparticles under Engine-like Conditions. Energ Fuel, 2014, 28(5), 3430-3441

5. Beach D.B., Rondinone A.J., Sumpter B.G., Labinov S.D., Richards R.K., Solid-State Combustion of Metallic Nanoparticles: New Possibilities for an Alternative Energy Carrier. J En Res Techn, 2007, 129, 29-32

6. Yanan G., Yi Syuen L., Li Q., Combustion of nanofluid fuels with the addition of boron and iron particles at dilute and dense concentration. Comb Flame, 2012, 159, 1732-1740

7. Rakhi N.M., Mousumi C., Parimal A.P., Nanofuels: Combustion, engine performance and emissions, Fuel, 2014, 120, 91-97

8. Jenkins T.P., Hanson R.K., Soot pyrometry using modulated absorption/emission. Comb Flame, 2001, 126, 1669-1679

9. Bohren C.F., Huffman D.R., Absorption and Scattering of Light by Small Particles, Wiley, New York, 1983, ISBN 9780471293408

10. Johnson P.B., Christy R.W., Optical constants of transition metals: Ti, V, Cr, Mn, Fe, Co, Ni, and Pd. Physical Review B, 1974, 9, 5056-5070

11. Henning T., Begemann B., Mutschke H., Dorschner J., Optical Properties of Oxide Dust Grains. Astron Astrophys Suppl Ser, 1995, 112, 143-149

12. Gordon S., Mc Bride B.J., Computer program for calculation of complex chemical equilibrium composition, rocket performance, incident and reflected shocks, and Chapman-Jouguet detonations. 1973, NASA SP-273

13. Dossett J., Totten G.E., ASM Handbook Vol. 4A, Steel Heat Treating Fundamentals and Processes, ASM International, 2013, ISBN 978-1-62708-011-8

14. Wen D., Song P., Zhang K., Qian J., Thermal oxidation of iron nanoparticles and its implication for chemical-looping combustion. J Chem Technol Biotechnol, 2011, 86, 375-380

15. Barin I., Thermochemical Data of Pure Substances 3rd ed., Wiley-VCH Verlag GmbH, Weinheim, Germany, 1995, ISBN 3-527-27812-5

16. Powell J., Petring D., Kumar R.V., Al-Mashikhi S.O., Kaplan A.F.H., Voisey K.T., Laser–oxygen cutting of mild steel. J Phys D Appl Phys, 2009, 42, 11

17. Huang Y., Risha G.A., Yang V., Yetter R.A., Effect of particle size on combustion of aluminum particle dust in air. Comb Flame, 2009, 156, 5-13

18. Liu F., Daun K.J., Snelling D.R., Smallwood G.J., Heat conduction from a spherical nano-particle: status of modeling heat conduction in laser-induced incandescence. Appl Phys, 2006, B 83, 355-382

19. Rai A., Park K., Zhou L., Zachariah M.R., Understanding the mechanism of aluminium nanoparticle oxidation. Combust Theor Model, 2006, 10, 843-859

20. Brandt O., Rajathurai A.M., Roth P., First observations on break-up of particle agglomerates in shock waves, Exper Fluid, 1987, 5, 86-94

21. Heywood J.B., Internal Combustion Engine Fundamentals, International Edition, 1988, McGraw-Hill, ISBN 0-07-100499-8

22. Zhao H., Ladommatos N., Optical diagnostics for in-cylinder mixture formation measurements in IC engines. Prog Energ Comb Sci, 1998, 24, 297-336

23. Lynch P., Krier H., Glumac N., A correlation for burn time of aluminum particles in the transition regime. Proc Comb Inst, 2009, 32, 1887-1893